

Constraints of the formation and abundances of methyl carbamate, a glycine isomer, in hot corinos

DIPEN SAHU,¹ SHENG-YUAN LIU,¹ ANKAN DAS,² PRASANTA GARAI,² AND VALENTINE WAKELAM³

¹*Academia Sinica Institute of Astronomy and Astrophysics, 11F of AS/NTU Astronomy-Mathematics Building, No.1, Sec. 4, Roosevelt Rd, Taipei 10617, Taiwan, R.O.C.*

²*Indian Centre for Space Physics, 43 Chalanika, Garia St. Road, Kolkata 700084, India*

³*Laboratoire d'astrophysique de Bordeaux, Univ. Bordeaux, CNRS, B18N, allée Geoffroy Saint-Hilaire, 33615 Pessac, France*

(Received Oct 2018; Revised Jan 2019; Accepted June 30, 2020)

Submitted to ApJ

ABSTRACT

Methyl carbamate $\text{CH}_3\text{OC}(\text{O})\text{NH}_2$ is an isomer of glycine. Quantum chemical analyses show that methyl carbamate is more stable isomer than glycine. Because of this, there could be a higher chance for methyl carbamate to exist in the interstellar medium as compared to glycine. Despite immense searches, till now glycine has not been detected in the ISM, therefore it is worthwhile to search its isomer methyl carbamate. In this paper, we present the constraints of methyl carbamate formation under the interstellar conditions. Large complex organic molecules are favorably produced in hot-corino environments of low mass protostars. We for the first time carried out astrochemical modeling focusing on the formation of methyl carbamate in physical conditions similar to hot-corino objects. Consequently, we examined ALMA archival data for existing spectral line observations toward hot corinos NGC1333 IRAS 4A2 and IRAS 16293B. Within the common spectral range towards these sources, we found three features are possibly related to the spectral transitions of methyl carbamate and consequently estimate the upper limit of column densities. Results of chemical modeling are consistent with the observational upper limit of estimated column density/abundance toward the sources. This may hint the validation of the proposed formation mechanism. Future observations using telescope like ngVLA may confirm the presence of MC toward the hot corinos.

Keywords: ISM:abundances –ISM:individual object(NGC1333 IRAS4A & IRAS16293-2422 B)–ISM:molecules–stars:formation –Astrochemistry

1. INTRODUCTION

Amino acids are the building blocks of life as it is the essential compound for protein formation. Miller (1953) from his experiments showed that many amino acids can be produced in the laboratory using electric discharge in an aqueous mixture of ammonia, methane, and dihydrogen. In a later examination, Khare et al. (1986) observed 16 amino acids from the acidic treatment of tholins, which is present in Titan's atmosphere. Various investigations have also been performed to detect amino acids in extraterrestrial objects. For example, a number of amino acids have been detected in the Murchison me-

teorite (Toshiki et al. 2017). Amino acids have also been found in comet 67P/Churyumov-Gerasimenko (Altwegg et al. 2016). All these studies suggest that the presence of amino acids could be quite ubiquitous in extraterrestrial environments.

To further explore the prebiotic chemistry, it is indispensable to study the simplest amino acids, glycine. Although extensive observational searches had been made, no conclusive detection of glycine in the interstellar medium (ISM) is reported (e.g., Kuan et al. 2003; Snyder et al. 2005). Various authors discussed the formation of glycine in the ISM using possible pathways and chemical modeling (e.g. Garrod 2013; Suzuki et al. 2018), but it remains illusive.

In the context of isomeric species, it is interesting to note that ISM molecules often form preferentially following the 'minimum energy principle (MEP)' (Guillemain

et al. 2014). The MEP predicts that thermodynamically the most stable isomer should be the most abundant. As an example, in the molecular clouds where C_2H_3N isomers have been detected - the more stable acetonitrile (CH_3CN) is found to be more abundant than methyl isocyanide (CH_3NC) and ketenimine (CH_2CNH). Similarly acetaldehyde (CH_3CHO) is more abundant than its isomeric counterpart vinyl alcohol (CH_2CHOH) (see Guillemin et al. 2014, and references therein). There could exist, however, some exceptions due to the difference in the efficiencies of their reactions (Lattalais et al. 2009). Loomis et al. (2015) further argued that MEP may not be generally applicable to interstellar chemistry and the formation of complex organic molecules (COMs). They suggested that in the ISM local environments play a major role for the formation of chemical species rather than thermodynamic stability of individual species. Nevertheless, it is worthwhile to examine the molecule of prebiotic important $C_2H_5O_2N$, of which three isomers are glycine (NH_2CH_2COOH), N-methylcarbamic acid ($CH_3NHCOOH$) and methyl carbamate ($CH_3OC(NH_2)O$). Quantum chemical studies of the energy stability showed that N-methylcarbamic acid (dipole moment ~ 1.2 Debye) is the most stable isomer among these three (Lattalais et al. 2011). To the best of our knowledge, N-methylcarbamic acid has never been searched in the ISM, maybe due to the unavailability of its spectroscopic data. On the other hand, methyl carbamate (MC) is the second stable isomer, 4 kcal/mole above the most stable isomer ($CH_3NHCOOH$) while glycine is ~ 10 kcal/mol above (Lattalais et al. 2011). In addition, MC¹ has a dipole moment of ~ 2.4 Debye, higher than N-methylcarbamic. Maybe for this reason, MC was searched toward the intermediate-mass protostar IRAS21391+58502 and the hot core W51e2 (Demmyk et al. 2004). However, no further detail or positive results are available in the literature.

Nonetheless, in the ISM, COMs formation are often described to be formed predominantly on the ice phase via radical-radical reactions (e.g., Garrod 2013). Motivated by these, we performed chemical modeling assuming that MC is formed through similar pathways and searched for possible signatures of MC in the protostellar hot corino sources NGC 1333 IRAS 4A2 and IRAS 16293-2422 B. Hot corinos are associated with low-mass star formation at its relatively early evolutionary stage. Due to the elevated temperature (> 100 K) in the vicinity of protostars, molecules in icy mantels come off to the

gas phase due to thermal desorption. For this reason, a large abundance of COMs are often observed in the gas phase toward hot-corino objects. Results from chemical modeling show that COMs formation more likely occurs during the warm-up phase in the star formation process (Garrod 2006). In this context, the hot-corino sources are good target to search for COMs such as MC. We model the formation of methyl carbamate in the hot-corino environments to study the possibility of its presence. We also present the ALMA observations of NGC 1333 IRAS 4A2 and IRAS 16293-2422 B towards of which we derived MC's column density upper limits being consistent with the chemical modeling results.

2. ASTROCHEMICAL MODELING

2.1. *The chemical model, NAUTILUS*

To estimate the formation of methyl carbamate in the ISM and particularly in the hot corino environment, we use the NAUTILUS chemical code. The details of its formalism are described in Ruaud et al. (2016). Using NAUTILUS one can compute the time-evolution of chemistry (called 0D) and also spatial distributions of species (called 1D; see Wakelam et al. 2014, for example). The chemical code considers the interaction between gas and grain and calculates the chemical evolution both in gas and on dust surfaces. The rate equation approximation is used in the code to estimate molecular abundances of species in the gas phase, dust surfaces and in the bulk of grain mantle (i.e., a three-phase model). For the dust surface chemistry, NAUTILUS considers only the physisorption of chemical species onto the dust surface and subsequent diffusion mechanism to produce new species due to chemical reactions/recombinations. The surface species can come to the gas phase via different desorption mechanisms including thermal desorption (temperature dependent), UV photodesorption, cosmic-ray induced evaporation, and chemical desorption (see Ruaud et al. 2016, and references therein).

2.2. *chemical network and methyl carbamate*

We developed a chemical network for the methyl carbamate starting from the kida.uva.2014 gas-phase network² and from the surface network described in Ruaud et al. (2016) for the surface processes, both updated from Wakelam et al. (2015, 2017); Hickson et al. (2016); Loison et al. (2016, 2017); Vidal et al. (2017). The starting network is the same network used in Wakelam et al. (2019). To these sets of network, we have added several relevant species and reactions

¹ Polarizability $6.6 \pm 0.5 \times 10^{24} \text{cm}^3$, CSID:11229, <http://www.chemspider.com/Chemical-Structure.11229.html> (accessed 02:52, Jun 24, 2020)

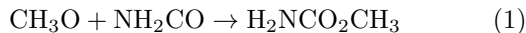
² (<http://kida.astrophy.u-bordeaux.fr>)

Table 1. Initial abundances with respect to total hydrogen nuclei

Species	Abundance
H ₂	5×10^{-1}
He	1.0×10^{-1}
O	1.76×10^{-4}
C ⁺	7.3×10^{-5}
N	2.14×10^{-5}
S ⁺	8×10^{-8}
Si ⁺	8×10^{-9}
Mg ⁺	7×10^{-9}
Cl ⁺	4×10^{-9}
Fe ⁺	3×10^{-9}
P ⁺	3×10^{-9}
Na ⁺	2×10^{-9}

for exploring the formation of MC. The added species are $s - \text{CH}_3\text{O}$, $s - \text{NH}_2\text{CO}$, $s - \text{H}_2\text{NCO}_2\text{CH}_3$ (MC), $s - \text{NH}_2$, $s - \text{CH}_3\text{OCO}$, $s - \text{CH}_3\text{CO}$, and $s - \text{HOCO}$ in the grain phase, with ‘s’ representing surface species. Along with these, gas-phase species corresponding to the grain phase species including some newly produced gas phase species are also considered. Initial abundances of elemental species (Das et al. 2015a) and reactions involving these species are summarized in Table 1 and Table 2, respectively.

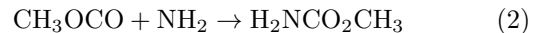
Carbamate compound is formally derived from carbamic acid (NH_2COOH). In terrestrial conditions, methyl carbamate is produced by the reaction of methanol and urea. This reaction, however may not be suitable for interstellar medium due to its extreme conditions such as very low pressure and temperature compared to the Earth atmosphere. For efficient formation of MC under ISM conditions, we consider the solid phase radical-radical reaction of CH_3O and NH_2CO :



We check the potential of this radical-radical reaction using quantum chemical calculations (B3LYP/6-311g++(d,p) method, Gaussian 09 software). The enthalpy of the reaction is found to be -80.79 Kcal/mol, i.e. the reaction is exothermic and can proceed on grain surface. Additionally, we assume the radical-radical reaction to be barrier-less. The methoxy radical CH_3O has been observed in the ISM (Cernicharo et al. 2012) and NH_2CO can form quite easily on grain surfaces (Ligterink et al. 2018). Pathways for CH_3O are already available in the network, and pathways for NH_2CO are shown in Table 2. CH_3O mainly forms on grain surfaces via recombination reactions (simplest molecule H_2 as well as COMs can form via this mechanism, see Sahu

et al. 2015; Das et al. 2016) of atoms (e.g., O) and radicals (e.g., CH_3); also it can be produced from CH_3OH as a result of hydrogen abstraction on grain surfaces. CH_3O is already present in our network and available in KIDA. Also, NH_2CO mainly form on grain surfaces via recombination reactions (Quénard et al. 2018) and hydrogen abstraction from species like NH_2CHO (Haupa et al. 2019). The binding energies of NH_2CO and CH_3O are considered to be 5160 K and 4400 K, respectively (Wakelam et al. 2017). Due to the high surface binding energies of the reactants, the radical-radical reaction (1) is unattainable at low temperature. At warm temperature (~ 100 K and higher) the radicals get enough mobility to activate the reaction on grain surfaces.

Another tentative reaction that can produce MC in the solid phase is:



This reaction was discussed by Lee et al. (2009), where they speculated CH_3OCO formation from the recombination of CH_3O and CO . They concluded that the reaction is unlikely under cold condition. Though this reaction may be relevant for hot-corino like temperature (> 100 K), we did not include this reaction in our network as the formation of CH_3OCO radical is not well known. Therefore, we have only considered Reaction (1) for solid phase production of MC. Due to various surface desorptions the solid phase MC can populate the gas phase, while no other gas phase production of MC is considered. We consider different kinds of desorption mechanisms (see section 2.1) and find that thermal desorption is the dominant mechanism for gas phase abundance of MC. As shown in Table 2, the destruction of MC occurs mainly due to ion-neutral reactions and photodissociation including cosmic ray dissociation. We have also considered MC being adsorbed back onto grain surface in our network.

From Table 2, we can see that NH_2CO formation is related to NH_2CHO (formamide) and HNCO (isocyanic acid). Also, CH_3NCO (methyl isocyanate) is another COM which is chemically related to HNCO (e.g., Gorai et al. 2020). As MC mainly from via NH_2CO radical, for the completeness of the chemical network we have to consider reactions related to NH_2CHO , HNCO , and CH_3NCO . Reaction pathways of these molecules are included in our network. In Table 2, we only noted some major reactions related to these molecules. Values of reactions rate constants vary over published articles. In our chemical network, we parameterized the major reactions (Table 2) following Gorai et al. (2020) and references therein. In Table 2, the gas phase reaction rate constants for MC are assumed to be sim-

Table 2. The chemical reaction network of methyl carbamate

Reactions	α	β	γ	Reaction type
$s - \text{CH}_3\text{O} + s - \text{NH}_2\text{CO} \rightarrow s - \text{H}_2\text{NCO}_2\text{CH}_3$	1.000e+00	0.000e+00	0.000e+00	surface
$s - \text{H}_2\text{NCO}_2\text{CH}_3 \rightarrow \text{H}_2\text{NCO}_2\text{CH}_3$	1.000e+00	0.000e+00	0.000e+00	surface
$s - \text{NH}_2 + s - \text{CO} \rightarrow s - \text{NH}_2\text{CO}$	1.000e+00	0.000e+00	2.100E+03	surface
$s - \text{NH}_2\text{CO} + s - \text{H} \rightarrow s - \text{NH}_2\text{CHO}$	1.000e+00	0.000e+00	0.000e+00	surface
$s - \text{NH}_2\text{CO} + s - \text{H} \rightarrow s - \text{HNCO} + \text{H}_2$	1.000e+00	0.000e+00	0.000e+00	surface
$s - \text{NH}_2\text{CO} + s - \text{H} \rightarrow s - \text{NH}_3 + \text{CO}$	1.000e+00	0.000e+00	0.000e+00	surface
$s - \text{NH}_2\text{CHO} + s - \text{H} \rightarrow s - \text{NH}_2\text{CO} + s - \text{H}_2$	1.000e+00	0.000e+00	2.500e+03	surface
$s - \text{HNCO} + s - \text{H} \rightarrow s - \text{NH}_2\text{CO}$	1.000e+00	0.000e+00	4.150e+03	surface
$s - \text{NH}_2\text{CO} \rightarrow \text{NH}_2\text{CO}$	1.000e+00	0.000e+00	0.000e+00	surface
$\text{H}_2\text{NCO}_2\text{CH}_3 + \text{Photon} \rightarrow \text{NH}_2\text{CO} + \text{CH}_3\text{O}$	1.380e-09	0.000e+00	1.730e+00	photo
$\text{H}_2\text{NCO}_2\text{CH}_3 + \text{CRP} \rightarrow \text{NH}_2\text{CO} + \text{CH}_3\text{O}$	1.500e+03	0.000e+00	0.000e+00	CRP
$\text{H}_2\text{NCO}_2\text{CH}_3 + \text{Photon} \rightarrow \text{NH}_2 + \text{CH}_3\text{OCO}$	1.380e-09	0.000e+00	1.730e+00	photo
$\text{H}_2\text{NCO}_2\text{CH}_3 + \text{CRP} \rightarrow \text{NH}_2 + \text{CH}_3\text{OCO}$	1.500e+03	0.000e+00	0.000e+00	CRP
$\text{H}_2\text{NCO}_2\text{CH}_3 + \text{C}^+ \rightarrow \text{C} + \text{COOCH}_4^+ + \text{NH}$	1.860e-09	1.000e+00	3.240e+00	Bi-mol
$\text{H}_2\text{NCO}_2\text{CH}_3 + \text{He}^+ \rightarrow \text{He} + \text{CH}_3 + \text{H}_2\text{NCO}_2^+$	3.080e-09	1.000e+00	3.240e+00	Bi-mol
$\text{H}_2\text{NCO}_2\text{CH}_3 + \text{H}_3^+ \rightarrow \text{H}_2 + \text{NH}_6\text{C}_2\text{O}_2^+$	3.510e-09	1.000e+00	3.240e+00	Bi-mol
$\text{H}_2\text{NCO}_2\text{CH}_3 + \text{H}^+ \rightarrow \text{NH}_2 + \text{COOCH}_4^+$	6.010e-09	1.000e+00	3.240e+00	Bi-mol
$\text{H}_2\text{NCO}_2\text{CH}_3 + \text{HCO}^+ \rightarrow \text{CO} + \text{NH}_6\text{C}_2\text{O}_2^+$	1.310e-09	1.000e+00	3.240e+00	Bi-mol
$\text{H}_2\text{NCO}_2\text{CH}_3 + \text{H}_3\text{O}^+ \rightarrow \text{H}_2\text{O} + \text{NH}_6\text{C}_2\text{O}_2^+$	1.530e-09	1.000e+00	3.240e+00	Bi-mol
$\text{CH}_3 + \text{HOCO} \rightarrow \text{CH}_3\text{OCO} + \text{H}$	1.000e-10	0.000e+00	8.004e+03	Bi-mol
$\text{H}_3^+ + \text{CH}_3\text{OCO} \rightarrow \text{CH}_3\text{COOH}^+ + \text{H}_2$	1.000e-09	-5.000e-01	0.000e+00	Bi-mol
$\text{HCO}^+ + \text{CH}_3\text{OCO} \rightarrow \text{CH}_3\text{COOH}^+ + \text{CO}$	1.030e-09	-5.000e-01	0.000e+00	Bi-mol
$\text{H}^+ + \text{CH}_3\text{OCO} \rightarrow \text{CH}_3\text{OCO}^+ + \text{H}$	1.000e-09	-5.000e-01	0.000e+00	Bi-mol
$\text{CO}^+ + \text{CH}_3\text{OCO} \rightarrow \text{CH}_3\text{OCO}^+ + \text{CO}$	1.440e-09	-5.000e-01	0.000e+00	Bi-mol
$\text{He}^+ + \text{CH}_3\text{OCO} \rightarrow \text{CH}_3\text{OCO}^+ + \text{He}$	1.000e-09	-5.000e-01	0.000e+00	Bi-mol
$\text{CH}_3\text{COOH}^+ + \text{e}^- \rightarrow \text{CH}_3\text{OCO} + \text{H}$	3.000e-07	-5.000e-01	0.000e+00	Bi-mol
$\text{CH}_3\text{OCO} + \text{CRP} \rightarrow \text{CO}_2 + \text{CH}_3$	4.000e+03	0.000e+00	0.000e+00	CRP
$\text{CH}_3\text{OCO} + \text{Photon} \rightarrow \text{CO}_2 + \text{CH}_3$	5.000e-10	0.000e+00	0.000e+00	photo
$\text{CH}_3\text{OCO}^+ + \text{e}^- \rightarrow \text{CH}_3 + \text{CO}_2$	1.500e-07	-5.000e-01	0.000e+00	Bi-mol
$\text{H}_2\text{NCO}_2^+ + \text{e}^- \rightarrow \text{NH}_2 + \text{CO}_2$	1.500e-07	-5.000e-01	0.000e+00	Bi-mol
$\text{NH}_6\text{C}_2\text{O}_2^+ + \text{e}^- \rightarrow \text{H} + \text{H}_2\text{NCO}_2\text{CH}_3$	1.500e-07	-5.000e-01	0.000e+00	Bi-mol
$\text{NH}_6\text{C}_2\text{O}_2^+ + \text{e}^- \rightarrow \text{NH}_2\text{CO} + \text{CH}_3\text{OH}$	1.500e-07	-5.000e-01	0.000e+00	Bi-mol
$\text{NH}_2\text{CHO} + \text{H} \rightarrow \text{H}_2 + \text{NH}_2\text{CO}$	1.000e-10	0.000e+00	3.1e+3/2.4e+3 **	Bi-mol
$\text{NH}_2\text{CO} + \text{H} \rightarrow \text{H}_2 + \text{HNCO}$	1.000e-10	0.000e+00	0.000e+00	Bi-mol
$\text{HNCO} + \text{H} \rightarrow \text{NH}_2\text{CO}$	1.000e-10	0.000e+00	5.050e+03	Bi-mol
$\text{NH}_2\text{CO} + \text{H} \rightarrow \text{NH}_2\text{CHO}$	1.000e-10	0.000e+00	0.000e+00	Bi-mol
$\text{NH}_2\text{CO} + \text{CRP} \rightarrow \text{NH}_2 + \text{CO}$	9.500e+03	0.000e+00	0.000e+00	CRP
$\text{NH}_2\text{CO} + \text{He}^+ \rightarrow \text{He} + \text{CO} + \text{NH}_2^+$	5.000e-01	2.450e-09	8.130e+00	Bi-mol*
$\text{NH}_2\text{CO} + \text{H}_3^+ \rightarrow \text{H}_2 + \text{NH}_2\text{COH}^+$	1.000e+00	2.790e-09	8.130e+00	Bi-mol*
$\text{NH}_2\text{CO} + \text{HCO}^+ \rightarrow \text{CO} + \text{NH}_2\text{COH}^+$	1.000e+00	1.130e-09	8.130e+00	Bi-mol*
$\text{NH}_2\text{CO} + \text{H}^+ \rightarrow \text{NH}_2 + \text{HCO}^+$	5.000e-01	4.730e-09	8.130e+00	Bi-mol*
$\text{NH}_2\text{CO} + \text{H}^+ \rightarrow \text{HCO} + \text{NH}_2^+$	5.000e-01	4.730e-09	8.130e+00	Bi-mol*
$\text{NH}_2\text{COH}^+ + \text{e}^- \rightarrow \text{HCO} + \text{NH}_2$	1.500e-07	-5.000e-01	0.000e+00	Bi-mol
$\text{NH}_2\text{COH}^+ + \text{e}^- \rightarrow \text{H} + \text{NH}_2\text{CO}$	1.500e-07	-5.000e-01	0.000e+00	Bi-mol
$\text{NH}_2\text{CHO} + \text{H} \rightarrow \text{H}_2 + \text{NH}_2\text{CO}$	1.000e-10	0.000e+00	1.500e+03	Bi-mol*
$\text{NH}_2\text{CO} + \text{H} \rightarrow \text{H}_2 + \text{HNCO}$	1.000e-10	0.000e+00	0.000e+00	Bi-mol*
$\text{NH}_2\text{CO} + \text{H} \rightarrow \text{NH}_2\text{CHO}$	1.000e-10	0.000e+00	0.000e+00	Bi-mol*
$\text{HNCO} + \text{H} \rightarrow \text{NH}_2\text{CO}$	1.000e-10	0.000e+00	3.000e+03	Bi-mol*
Gas phase reaction parameterized				
$\text{CH}_3 + \text{HNCO} \rightarrow \text{CH}_3\text{NCO} + \text{H}$	1.000e-11	0.000e+00	0.000e+00	Bi-mol
$\text{NH}_2 + \text{H}_2\text{CO} \rightarrow \text{NH}_2\text{CHO} + \text{H}$	1.000e-12	-2.560e+00	4.880e+00	Bi-mol

Note: α , β , γ are rate constants, and rate coefficients are calculated based on reaction types as mentioned in column 5. The formulae that are used to calculate rate coefficients different categories of reactions are the following, CRP: $\kappa = \alpha\zeta$, where ζ is cosmic-ray ionization rate; photo: $\kappa = \alpha\exp(-\gamma A_\nu)$; Bi-mol: $\kappa(T) = \alpha(T/300)^\beta\exp(-\gamma T)$; and Bi-mol*: $\kappa(T) = \alpha\beta(0.62 + 0.4767\gamma(300/T)^{0.5})$. **We consider this values for model 1 and model 2 respectively. For ‘surface’ reactions, the diffusion barrier to binding energy ratio is considered to be 0.5.

ilar to those for HCOOCH_3 . We consider only typical ion-neutral gas phase destruction pathways for MC. Also, tentative pathways for the newly produced species (e.g., CH_3OCO , CH_3COOH^+) are included for the completeness of the chemical network. Reaction rate constants are assumed similar to CH_3NCO for CH_3OCO and related species. We have added a few gas-phase destruction pathways (ion-neutral) for NH_2CO following NH_2CN . Gas phase reactions (neutral-neutral) of NH_2CO and H are taken from [Gorai et al. \(2020\)](#).

Since the reaction pathways for the main constituents of MC (NH_2CO and CH_3O) are incorporated, the network can be considered complete for investigating the MC formation. If there are other reaction routes for the production of MC, in that case, assuming no major destruction of MC from unknown pathways, the current network would provide at least an estimate of the lower limit of MC abundance using the astrochemical modeling.

2.3. Physical models

To simulate the chemistry of MC, we consider the inner region of a low mass star forming core from its collapsing parent molecular cloud core to the subsequent warm-up phase due to YSO heating. Two physical models are adopted for mimicking the emergence of a hot corino. Model 1 is a simple toy model in which the cloud core is initially assumed to be at 8 K with a density of $2 \times 10^4 \text{ cm}^{-3}$, and it evolves for 10^6 years in the prestellar phase. During the collapse phase, the density increases linearly to 10^8 cm^{-3} over a timescale of $\sim 2.1 \times 10^5$ years. At the end of the collapse phase, the dust temperature rises to 300 K (warm-up phase) within this period (e.g. [Viti et al. 2004](#); [Garrod 2006](#)). The temperature during the warm-up phase is assumed to increase linearly with time. At this phase, dust and gas is well coupled, and we assume gas and dust temperatures to be the same.

We further draw, as Model 2, the physical model from [Aikawa et al. \(2008, Fig 5 for 15 AU, in their work\)](#) which is based on a somewhat more realistic one-dimensional numerical radiation-hydrodynamical calculation. In Model 2, a static density ($2.0 \times 10^4 \text{ cm}^{-3}$ at 8 K) evolution for 10^6 years is assumed before the collapse and warm-up of the parent molecular cloud. The warm-up time in this model is very short ($\sim 9 \times 10^4$ years) compared to Model 1. Additionally, it warms up very quickly, though the final temperature is ~ 253 K, it reaches ~ 228 K only after a warm-up of 2.0×10^4 years. Dust and gas temperature are considered to be the same throughout the evolution.

Depending on the gas density in the molecular cloud the extinction coefficient (A_V) may vary, here we consider A_V varies according to the relation ([Das et al. 2015](#), and references therein):

$$n_H = n_{H0} [1 + (\sqrt{n_{H\text{max}}/n_{H0}} - 1) A_V / A_{V\text{max}}]^2 \quad (3)$$

where, n_{H0} is the initial density and $n_{H\text{max}}$ is the maximum density of the molecular cloud; $A_{V\text{max}}$ is the maximum visual co-efficient deep inside the cloud corresponding to the maximum density. In both our physical models, A_V is assumed to reach a maximum value 150 from a initial value of 10. A constant cosmic-ray ionization rate (ζ) of $1.3 \times 10^{-17} \text{ s}^{-1}$ is assumed throughout the simulations.

2.4. Results of modeling

Figure 1 displays the chemical evolution of MC abundance (with respect to H_2) obtained from the two adopted physical models. The top panels corresponds to the physical Model 1 while the bottom ones to Model 2. It is evident, based on Figure 1, that MC forms during the warm up phase and thermally desorbs into the gas phase. However, depending on the physical conditions of the models, the fractional abundances may vary. As introduced earlier, in our network we do not have gas-phase reactions which can directly produce MC. Its gas phase abundance mainly comes from the thermal desorption of the species which forms in the solid phase through the radical-radical reaction of CH_3O and NH_2CO .

The binding energies greatly affects the mobility of radicals and consequently the formation of molecules on the grain surface. Due to the high binding energies of CH_3O and NH_2CO , MC does not form effectively even in luke-warm (~ 30 K) conditions. Furthermore, since we assume a high binding energy (~ 10000 K, considered similar to glycine, [Garrod 2013](#)) for MC, it desorbs to the gas phase at high temperatures >100 K. As an example, for Model 1, MC starts major desorption at temperature ~ 150 K while reaches its peak gas phase abundance at temperature ~ 220 K. These temperature values are highly dependent on the binding energy of MC. [Garrod \(2013\)](#) considered the binding energy of MC to be 7610 K. To check the effect of binding energies, we consider two values 10000 K and 7610 K, and the results are shown in Figure 2. For a binding energy of 7610 K, major desorption of MC occurs at a temperature ~ 110 K while it reaches its peak gas phase abundance at a temperature ~ 160 K. We can see that the evolution curve of MC shifts to the high-temperature side of the warm-up region for a higher value of binding energy. So, the production of MC would be favored in hot-corino

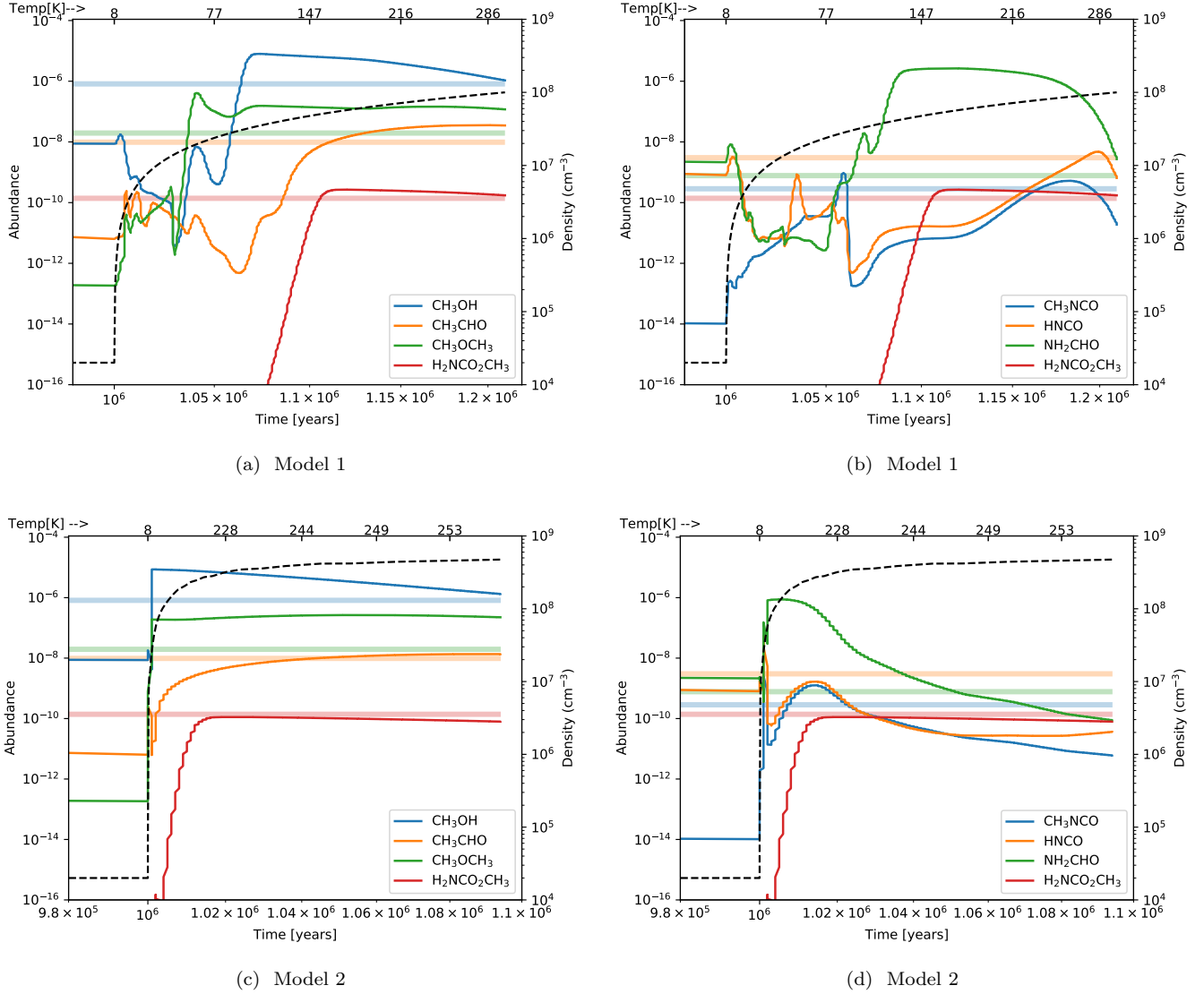


Figure 1. Time evolution of chemical species during the warm-up phase (after an initial period of 10^6 years). Upper panels show the results from physical model 1, and lower panels show the results from physical model 2. The dashed lines show the density evolution and the upper x-axis shows the temperature variation with time. Observed abundances of molecules towards I16293B are displayed in panels by solid-faint, colored lines with their widths representing 20% uncertainties.

(~ 110 K) environments and below this temperature MC production is substantially low.

To check the consistency of modeling compared to other well known COMs, we also show the chemical evolution of CH_3OH , CH_3CHO and CH_3OCH_3 . These COMs are well abundant in hot-corino environments and have well-established pathways; therefore it is meaningful to compare the MC abundance with those of these COMs. CH_3OH is the most abundant ($\sim 10^{-6}$) COMs in hot-corino environments. Since the estimation of hydrogen density involves many uncertainties (mainly due to dust opacity), the abundances of COMs are often described comparing to CH_3OH . Also, CH_3OCH_3 mainly

Table 3. The fractional abundances of chemical species as obtained from chemical modeling.

Molecule	Model 1	Model 2
CH_3OH	1.1e-06	1.4e-06
CH_3CHO	3.6e-08	1.4e-08
CH_3OCH_3	1.3e-07	2.3e-07
CH_3NCO	3.2e-10	1.2e-09
HNCO	3.6e-09	1.8e-09
NH_2CHO	2.7e-09	1.0e-09
$\text{H}_2\text{NCO}_2\text{CH}_3$	1.7e-10	0.9e-10

forms on grain surfaces similar to the assumed grain-

surface origin of MC, therefore it would be worthy to compare with MC. CH_3CHO forms in both gas and grain phase. Additionally, interferometric observations of these molecules are available at comparable resolution toward the hot corinos that we discuss in this paper (e.g., Sahu et al. 2019; Su et al. 2019; Drozdovskaya et al. 2019, and references therein). The observational results help us to better constrain the chemical modeling. In addition to these COMs, we consider NH_2CHO , HNCO , CH_3NCO which may be related to the formation of MC (see section 2.2).

Figure 1 shows the chemical evolution of the molecules for two different sets of physical conditions. For Model 1, we can see that the observed fractional column densities (w.r.t hydrogen) of molecules likely match the modeled abundances around a time $\sim 1.2 \times 10^6$, i.e. $\sim 2 \times 10^5$ years of warm-up. We estimated the best fit time focussing more on CH_3OH , MC and NH_2CHO . Though, for CH_3CHO and CH_3OCH_3 best time may be near to 1.1×10^6 years but at this time model abundance of NH_2CHO differs by orders of magnitude from observational value. So, we choose 1.2×10^6 years as the best-fit time for Model 1. The fractional abundances at this stage are noted in Table 3. In the case of Model 2, the temperature quickly crosses over 100 K over a short time-scale ($\sim 10^4$ years). For Model 2, we noted down the abundances (Table 3) after this short-time and within the final time of evolution. The model abundances are quite similar in both models except for CH_3NCO , which differ by an order of magnitude from each other. We note that the duration of the warm-up phase, in addition to the density profile, may severely affect the chemistry. The quicker and shorter warm-up in Model 2 affects the production of both CH_3NCO and HNCO (formation pathways of which are closely linked) differently than in Model 1. The results of modeling and observations are further compared and discussed in Section 4.

3. OBSERVATIONAL HINTS

Earlier we (Figure 2 of Sahu et al. 2019) have found forest of spectral transitions towards the hot-corino object NGC1333 IRAS 4A2. From a subsequent spectral search, we speculated the possible signatures of methyl carbamate towards IRAS 4A2. To check whether the transitions of MC are present in other line rich sources, we searched ALMA archive for existing spectral observations in the range 349.8-351.6 GHz, the observed window towards NGC133 IRAS 4A2. We found one of the well known hot-corino object, IRAS16293-2422 has been observed in the same frequency range (project id: ALMA#2013.1.00278.S). The spectral emission towards

the sources are strikingly similar and possible MC transitions (see Table 4) are present, too, in IRAS16293-2422 B. In this section, we briefly discuss the search of MC towards these hot corinos and also discuss the presence of relevant COMs.

3.1. IRAS 4A2

The NGC 1333 IRAS 4A (IRAS 4A hereafter) is one of the first known hot corino (Bottinelli et al. 2004) located in the Perseus molecular cloud at a distance of ~ 293 pc (Ortiz-León et al. 2018; Zucker et al. 2018). Bottinelli et al. (2004) recognized IRAS 4A as a Class 0 source and reported the presence of COMs, including HCOOCH_3 , HCOOH , and CH_3CN based on IRAM -30m telescope observations at angular resolutions ranging from $10''$ to $24''$. As IRAS 4A is in fact a protobinary system consists of two protostellar sources IRAS 4A1 and IRAS 4A2 at a separation of $1.''8$ (Looney et al. 2000; Reipurth et al. 2002), the ‘‘hot corino’’ signatures from single dish observations by Bottinelli et al. (2004) could not be attributed to the individual cores A1 and A2. While later observations (Persson et al. 2012) found that A2 harbors a hot corino, it is only recently that Sahu et al. (2019) discussed the possibility of A1 to host a hot-corino atmosphere.

In brief, the ALMA observations carried out in Sahu et al. (2019) and Su et al. (2019) deployed seven spectral windows, including one broadband window centered at 350.714 GHz whose bandwidth and spectral channel width are 1.875 GHz and 976 kHz ($\sim 0.84 \text{ km s}^{-1}$), respectively. The synthesized beam size of this spectral data cube is $\sim 0.''3 \times 0.''2$ (PA = -6.45°), sufficient for resolving the two cores A1 and A2, and the rms noise level (σ) is 3 mJy beam^{-1} ($\sim 0.5 \text{ K}$). The dust-continuum emission towards IRAS 4A2 is predominately optically thin and from the 2D Gaussian fittings, the extent of the compact component of dust is found to be $\sim 0.''27$ (see Table 1 of Sahu et al. 2019). Assuming, $\kappa_\nu=0.0182 \text{ cm}^2\text{g}^{-1}$ (Jørgensen et al. 2016), the average (from extended and compact emission) hydrogen column density is $\sim 2.5 \times 10^{25} \text{ cm}^{-2}$.

To analyze the spectra, we used CASSIS (developed by IRAP-UPS/CNRS- <http://cassis.irap.omp.eu>) software as well as the JPL (Pickett et al. 1998) and CDMS (Müller et al. 2001, 2005) databases. The spectroscopy data of MC that are available in JPL was studied by Ilyushin et al. (2006). The spectra towards IRAS 4A2 are extracted from a region similar to beam size around the peak position of dust-continuum. The line identifications are performed by assuming the systematic velocity to be 6.9 km s^{-1} (Sahu et al. 2019, and references therein). In the appendix section we show the

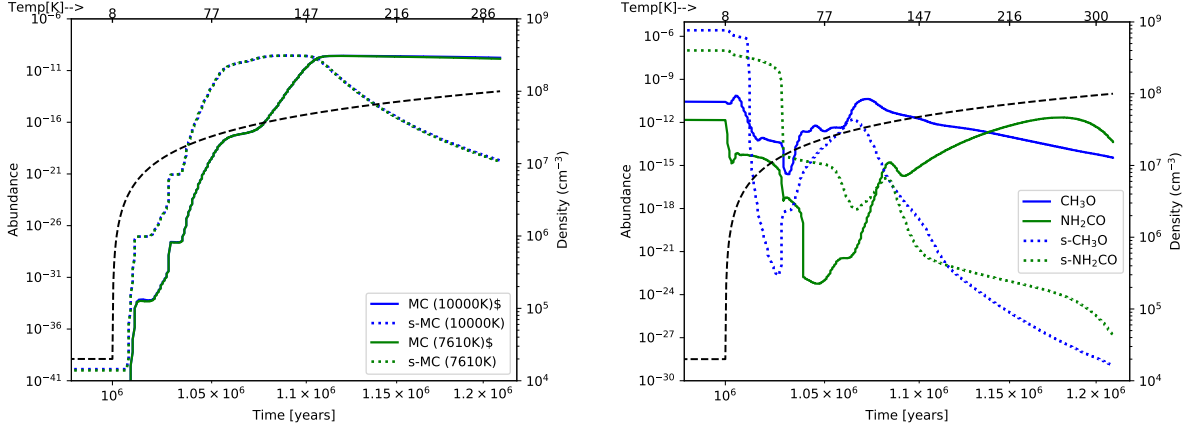


Figure 2. Left: Evolution of MC is depicted for various values of binding energies ; Right: Evolution of major radicals, NH_2CO and CH_3O (using Model 1 for both left and right panels

). Dotted lines show abundances in grain/dust surface and solid lines are for gas phase abundances. The dashed lines show the density evolution and the upper x-axis shows the temperature variation with time.

Table 4. Methyl carbamate transitions

Species	Transition (N Ka Kc v F)	Frequency (MHz)(Error)	E_u (K)	$A_{ij}(\text{s}^{-1})$
$\text{H}_2\text{NCO}_2\text{CH}_3$	(20,15,5,3,20 - 19,14,6,3,19)	349907.88 (0.0157)	322.69	9.22E-4
$\text{H}_2\text{NCO}_2\text{CH}_3$	(18,16,2,2,19 - 17,15,2,2,18)	351056.46 (0.0098)	147.42	1.11E-3
$\text{H}_2\text{NCO}_2\text{CH}_3$	(18,16,3,1,18 - 17,15,3,1,17)	351102.99 (0.0090)	147.38	1.11E-3
$\text{H}_2\text{NCO}_2\text{CH}_3$	(18,16,2,0,18 - 17,15,3,0,17)	351162.83 (0.0092)	147.42	1.11E-3
$\text{H}_2\text{NCO}_2\text{CH}_3$	(22,14,9,3,22 - 21,13,8,3,21)	351232.91 (0.0124)	329.02	7.93E-4

Note: This list contains only the main transitions that are discussed in the text, transition-multiplicities are present around these frequencies.

synthetic LTE spectra, in which at around 20 frequencies there are 106 MC transitions for the frequency range under consideration. We find that for $T_{ex} = 100$ K and 300 K, respectively, three and five emission features are at the level of 2σ or at best 3σ , where σ is rms noise of the observed spectra. There are multiple transitions around the frequencies of those emission features (see appendix, Table C.1). Representative transitions around those emission features are listed in Table 4. These transitions are useful for estimating the upper limit of the MC column densities in the observed spectra. At $T_{ex} = 100$ K, among the three emission profiles (see upper panel, Figure 3), one appears fully blended (351056.456 MHz) and the other emission features (351103.016 MHz, 351162.862 MHz) may be partially blended. For $T_{ex} = 300$ K, those three lines remain useful for estimating the upper limits. Additionally, two higher E_u (~ 320 K) line appear in the spectra which are fully blended (see Figure in Appendix section B). Column density estimations are made with those two temperature conditions.

The Einstein coefficients (A_{ij}) of all those major transitions are found to be $> 7 \times 10^{-4} \text{ s}^{-1}$. The syn-

thetic spectrum generated by CASSIS with a FWHM of $\sim 2.0 \text{ km s}^{-1}$ (considering an average Gaussian width $\sim 1 \text{ km s}^{-1}$, as reported by Sahu et al. 2019), a column density of $2.5 \times 10^{15} \text{ cm}^{-2}$, an excitation temperature of 100 K, and a source velocity of 6.9 km s^{-1} could reproduce the observed spectra. The E_u of these transitions are around ~ 147 K, it is therefore difficult to estimate the rotational temperature. We choose another typical excitation temperature, 300 K, to estimate the column density. At this temperature, a column density $\sim 7 \times 10^{15} \text{ cm}^{-2}$ could reproduce the observed spectral features. The transition around 351056 MHz is possibly blended with $\text{D}_2\text{C}_2\text{O}$ and aGg'-glycol. However, we could not quantitatively estimate the percentage of blending from these species as within the frequency range of the spectral window there are not enough transitions of those species to constrain their presence and abundances. The rest two transitions of MC are partially blended with intense transitions from other species, and the transition around 351162.862 MHz is estimated at a level $\sim 3\sigma$. Considering these limitations, we only estimate the upper limit of MC from the observational data set.

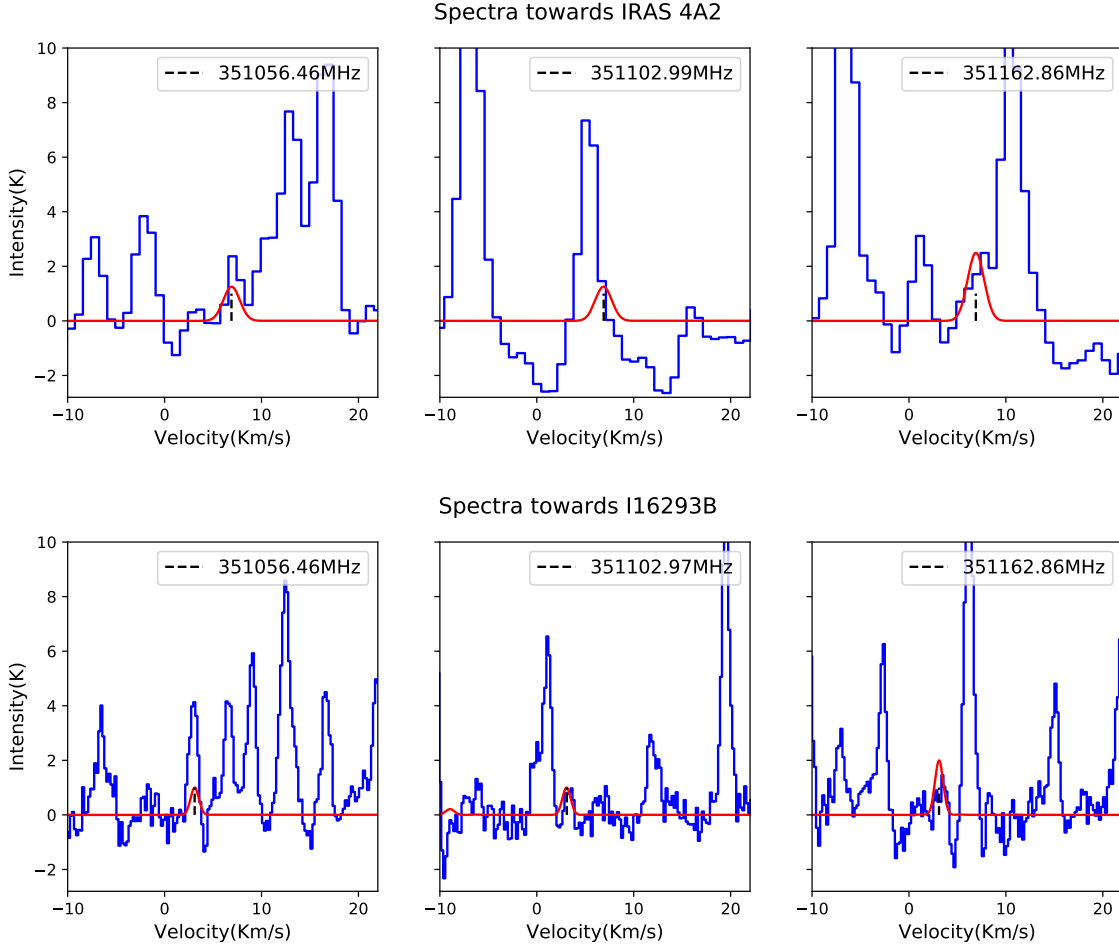


Figure 3. The observed spectral transition of methyl carbamate tentatively detected towards IRAS 4A2 and I16293 are plotted in blue. The synthetic spectra estimated based on the LTE assumption are over-plotted in red. The dotted lines represent the systematic velocity, and the frequencies of transition are noted in the panels.

It is relevant to mention the observed column densities of CH_3OH and CH_3CHO for comparison with methyl carbamate. Sahu et al. (2019) found that CH_3OH line emission may be optically thick and provide a lower limit for column density. So, to get the column density of CH_3OH , we use the observed column density of $^{13}\text{CH}_3\text{OH}$ (see Table 3 of Sahu et al. 2019) and use $^{12}\text{C}/^{13}\text{C}$ ratio $\simeq 35$ (Jørgensen et al. 2016), the resultant column density is $1.12 \times 10^{19} \text{ cm}^{-2}$. CH_3CHO line emission is also found to be optically thick, so to get the likely column density of it, we use $\text{CH}_3\text{OH}/\text{CH}_3\text{CHO}$ ratio (~ 83) towards I16293B (see listed column densities by Drozdovskaya et al. 2019), and the estimated column density towards IRAS 4A2 found to be $1.35 \times 10^{17} \text{ cm}^{-2}$; this value is consistent with the observed lower limit, $3.86 \times 10^{16} \text{ cm}^{-2}$ towards IRAS 4A2. Additionally, among other COMs, CH_3OCH_3 mainly produce in ISM on grain/ice surface, found to be present towards IRAS 4A2 (López-Sepulcre et al. 2017). Using an excitation condition from the earlier work ($T_{\text{ex}} \sim 130 \text{ K}$), we found

CH_3OCH_3 column density to be $\sim 9 \times 10^{16} \text{ cm}^{-2}$. These observational values are helpful for comparing with the chemical model results.

3.2. IRAS 16293

IRAS16293-2422 (IRAS16293/I16293 hereafter) is a hot corino source similar to IRAS 4A and also a protobinary consists of IRAS 16293A and IRAS 16293B. The binary protostars are separated by $5.1''$ (620 AU; see Jørgensen et al. 2016, and references therein). The source I16293B is chemically rich and the dust continuum is optically thick within a scale of 50 AU. We choose I16293B for our analysis as it is likely a face-on disk system and consequently the line widths are narrow. I16293A likely represents an edge-on system and its molecular line widths are comparatively broad. Jørgensen et al. (2016) found that the lines (FWHM $\sim 1 \text{ km s}^{-1}$) toward I16293B is five times narrower than I16293A, and this narrow line-width is helpful for

detecting lines with less line confusion. I16293B therefore is an ideal target to search for MC.

The data towards the source were taken from ALMA archive and imaged with the highest possible spectral resolution using CASA pipeline analysis. The whole data description can be found in Jørgensen et al. (2016) and we used only the 12m data, suitable to resolve the source without the missing-flux problem. The synthesized beam size for the dust-continuum map is $\sim 0''.63 \times 0''.39$ (Position angle = -79.92°); this is similar to the beam size for spectral cube. Jørgensen et al. (2016) argued that at its peak location, the dust continuum emission is optically thick and consequently the author chose a one-beam offset position from the continuum peak for extracting spectra. Assuming the dust emission at the offset position is optically thin, N_{H_2} found to be $\sim 1.2 \times 10^{25} \text{ cm}^{-2}$. Therefore, we choose a circular region similar to the observing beam ($0''.5$) around a position one offset away from continuum peak along the south west direction. Spectra from this position are expected to be least affected by the optical depth effect. Jørgensen et al. (2016) reported a rms noise level of $7\text{-}10 \text{ mJy beam}^{-1}$ ($\leq 0.6\text{K}$), where the channel width is 0.244 MHz ($\sim 0.2 \text{ km s}^{-1}$). With this educated estimation, we used the ‘statcont’ algorithm (Sánchez-Monge et al. 2018) to get the continuum subtracted emission. Line identification was done in same manner as described for IRAS 4A2, and we adopted a systematic velocity of $\sim 3.1 \text{ km s}^{-1}$ (Jørgensen et al. 2011). We found that, for excitation temperatures of 100 K and 300 K , respectively, the column densities of $1.0 \times 10^{15} \text{ cm}^{-2}$ and $2.3 \times 10^{15} \text{ cm}^{-2}$ best match with the observed spectral features, assuming FWHM $\sim 1 \text{ km s}^{-1}$. Additionally, the observed column densities for CH_3OH , CH_3CHO and CH_3OCH_3 are 1.0×10^{19} , $1.2 \times 10^{17} \text{ cm}^{-2}$, and 2.4×10^{17} respectively (Jørgensen et al. 2016, 2018). Figure 3 (lower panel) shows the tentative emission features of MC towards I16293B, assuming an excitation temperature of 100 K .

We note that for IRAS 4A2 all the spectral features of MC are either partially or fully blended due to low spectral resolutions. On the other hand, for I16293B, the 351103 MHz & 351162 MHz lines of MC seem to be resolved and non-blended. We choose the 351103 MHz line to check the emission map corresponding to this transition. The integrated emission map related to the transition is shown in Figure 4. Although the emission features presented in this paper are not sufficient yet for claiming a tentative detection of MC as there are only a limited number of transitions with their features being weak and blended. These emission features, however,

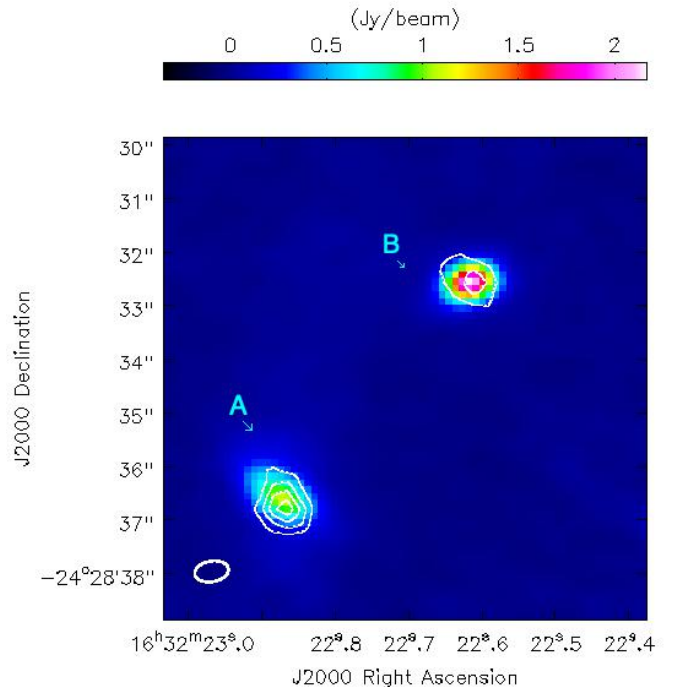


Figure 4. Integrated emission map (contours) of the 351103MHz MC transition towards I16293 overplotted with continuum emission map (color). We note that the integrated MC emission is localized around the hot corino I16293B. We note that toward I16293A, although the signal-to-noise ratio is high, we cannot solely attributed the integrated emission to MC given the different Vlsr and line contamination. Contours are $5, 10, 15\sigma, \dots$, where $\sigma = 6 \text{ mJy beam}^{-1} \text{ km s}^{-1}$.

are sufficiently good for estimating an upper limit of MC.

4. DISCUSSIONS AND CONCLUSIONS

In this paper we present the astrochemical modeling of methyl carbamate and its search toward line-rich hot-corino sources IRAS 4A2 and I16293B. Under the physical conditions that are described in the text, we can closely reproduce the observed fractional abundance of molecular species. Since obtaining the hydrogen column density from dust emission involves various uncertainties, we calculated the column density ratios of MC with respect to well known COMs, such as CH_3OH , CH_3CHO , CH_3OCH_3 assuming these COM species reside in the same volume. For both sources, the hydrogen column densities are $\sim 10^{25} \text{ cm}^{-2}$, and methanol column densities are $\sim 10^{19} \text{ cm}^{-2}$. Since the dust continuum is assumed to be optically thin, hydrogen column densities presented in the text are lower limits of hydrogen column densities. Therefore, the upper limit of methanol abun-

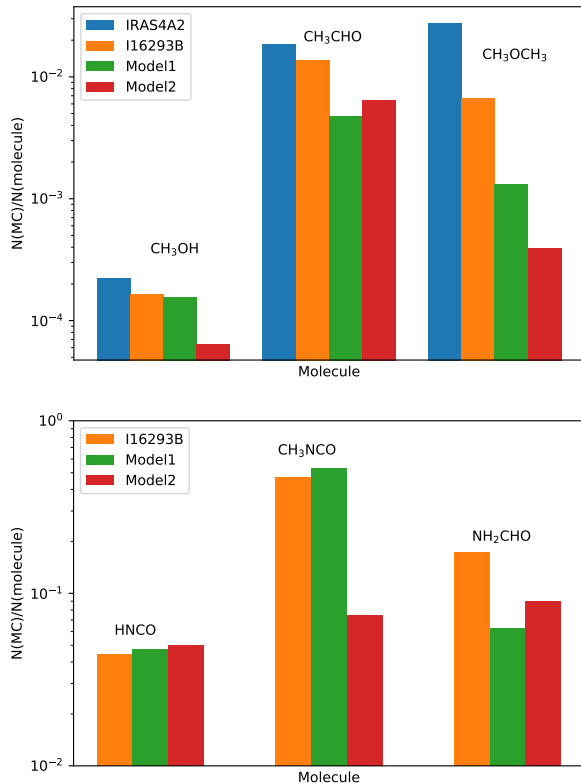


Figure 5. Plots shows the relative abundance of methyl carbamate (MC) with respect to CH₃OH, CH₃CHO and CH₃OCH₃ obtained from observations (I16293B, IRAS 4A2) and chemical modeling, Model 1 and Model 2. The observational values for MC are the average of estimated range of column densities.

dance (w.r.t. hydrogen) is of the order of 10^{-6} . In the chemical modeling, for different physical conditions, we obtain methanol abundances of $\sim 10^{-6}$. Therefore, the results of the chemical models are suitable for describing the major abundant COM, methanol. We compare the observed fractional abundances of these COMs with MC in Figure 5. We can see that the observed and model abundances of MC comparing to those COMs match well within an order of magnitude. This effectively gives us the idea of the MC abundance relative to those well abundant COMs.

Since one main constituent of MC is NH₂CO radical, we consider species- CH₃NCO, HNCO, NH₂CHO which are closely linked with NH₂CO and therefore MC. Towards I16293B, their abundances have been measured at a comparable resolution (see Drozdovskaya et al. 2019, and references therein). For IRAS 4A2, some of these species have been observed at much coarser angular resolutions (e.g., Taquet et al. 2015, and references therein), and there may be large uncertainties in column density estimation due to beam dilution factor. Therefore, com-

parison between the model and observed abundances are shown only for I16293B (Figure 5).

We can see that the modeled and observed fractional abundances of MC with respect to CH₃OH and CH₃CHO closely match. These molecules are major abundant molecules in hot corinos, so the abundance ratio of these molecules to MC can be helpful to gauge the MC abundances in hot-corino environments. CH₃OCH₃ is overproduced in our chemical modeling, resulting in a order of magnitude difference between observed and modeled abundance. As the radical CH₃O, a major constituent of MC, is mainly produced with reactions related to CH₃OH, so CH₃OCH₃ may not be a good species for estimating the MC abundance. On the other hand, modeled abundances ratios of MC and species like HNCO, CH₃NCO, NH₂CHO are mostly in agreement with the observed results except for CH₃NCO estimation of Model 2. Due to very short and quick warm-up time scale of Model 2, this kind of differences may arise. However, the results suggest that HNCO, CH₃NCO, NH₂CHO maybe helpful for estimating MC abundances. Significance of the modeling results is that the upper limit of observed column densities ($\sim 10^{15}$ cm⁻²) of MC (an glycine isomer) roughly consistent with the modeled abundances. For the first time, we performed the observational search of MC and chemical modeling. Results of chemical modelling suggest that species like CH₃OH, HNCO, CH₃NCO, NH₂CHO may helpful for estimating possible abundance of MC, using this estimations MC can be searched toward hot corinos.

MC can be searched using modern telescope facility like ALMA and future telescopes like ngVLA. To avoid line confusion problem, MC can be searched using high sensitive ALMA spectral line observations in lower frequencies (84 -116 GHz, Band 3). However, it should be noted that for larger molecules like MC, the transitions are very weak in the range of ALMA’s spectral coverage. Rotational transitions of lighter molecules mostly fall within the mm-submm spectral range, so spectral confusion limit may reach in short time (~ 1 hour) and it may make identification of MC difficult. Since, rotational transition of comparatively smaller molecules (e.g., CH₃OH) do not fall in centimeter wavelength range, this wavelength regime is comparatively clearer and therefore reduces the level of line-confusion. Therefore, future astronomical telescope like ngVLA may be helpful for detecting the glycine isomer, MC. Using the MC column-density upper limit, we find that the strongest transition around 43 GHz have intensity ~ 0.3 mJy. Assuming, beam size fill the source, a sensitivity of ~ 0.05 mJy can be achieved by ngVLA approximately in 10 hours of integration time (McGuire et

al. 2018). Therefore, it is possible to detect MC using ngVLA toward the hot corinos. Detection of MC in the ISM may shed light on the long standing problem to understand glycine/prebiotic chemistry in the ISM.

Acknowledgment: We thank the reviewers for their constructive comments and suggestions. D.S. acknowledges ASIAA post doctoral research fund, also thanks Dr. Bhalamurugan Sivaraman for helpful discussions. S.Y.L. acknowledges the support by the Minister of Science and Technology of Taiwan (MOST 107-2119-M-001-041). A.D. would like to acknowledge ISRO re-

spond project (Grant No. ISRO/RES/2/402/16-17) for partial financial support and Grant-In-Aid from the Higher Education Department of the Government of West Bengal. This paper makes use of the following ALMA data: ADS/JAO.ALMA#2015.1.00147.S & ALMA#2013.1.00278.S. ALMA is a partnership of ESO (representing its member states), NSF (USA) and NINS (Japan), together with NRC (Canada) and MoST and ASIAA (Taiwan) and KASI (Republic of Korea), in cooperation with the Republic of Chile. The Joint ALMA Observatory is operated by ESO, AUI/NRAO and NAOJ.

APPENDIX

A. SYNTHETIC LTE SPECTRA TO SEARCH FOR MAJOR SPECTRAL TRANSITIONS OF MC

Figure A.1 shows the synthetic LTE spectra (using CASSIS software) of MC for column densities of $1.0 \times 10^{15} \text{ cm}^{-2}$ and $2.3 \times 10^{15} \text{ cm}^{-2}$, respectively for excitation temperatures of 100 K and 300 K towards I16293B; source size was assumed to be $0.''5$. These figures give an idea about the major emission signatures of MC to look for. For $T_{ex}=100$ K and 300 K, respectively, there are three and five major transitions at a label of 2σ (rms) or higher. These transitions are listed in Table 4. Based on these transitions, the upper limit of MC column densities are estimated from the observed spectra towards the hot corinos.

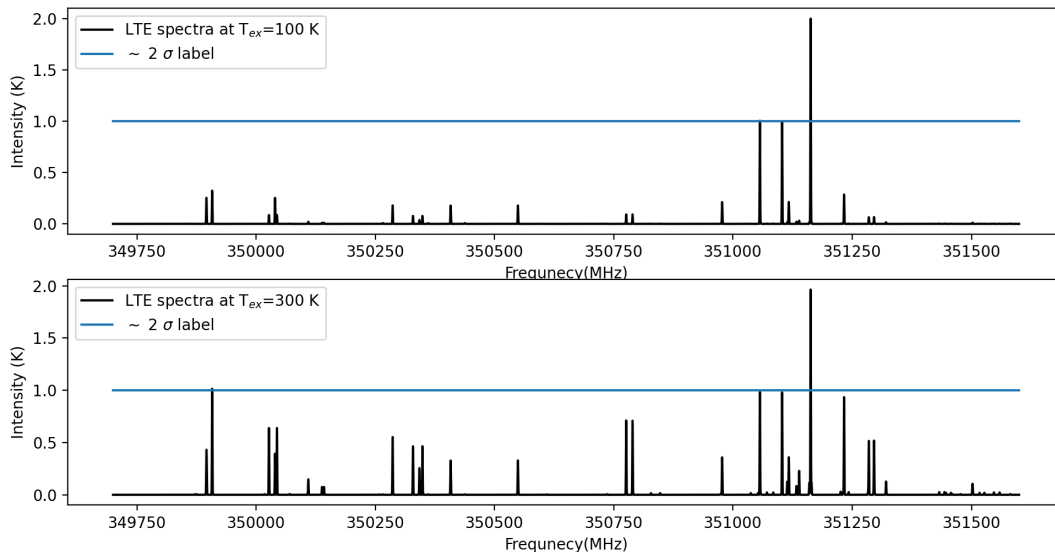


Figure A.1. A typical LTE synthetic spectra is displayed considering excitation temperature 100K and 300K. Straight lines shows 2σ level of the observed spectra towards IRAS16293B.

B. LTE SPECTRA FOR $T_{EX}=300$ K

Figure B.1 and B.2 show the LTE synthetic spectra of MC towards IRAS 4A2 and I16293B respectively, for an excitation temperature of 300 K. We searched for all MC lines having $E_u < 500$ K. As the emission features of MC are very weak and blended, the rotational temperature can not be estimated from the observed spectra. Therefore, we assumed two typical temperatures, 100 K and 300 K, for estimating the upper limit of MC column densities. The LTE spectra for 100 K are already shown in figure 3. We can see that for $T_{ex}=300$ K few high-temperature lines appear in

the spectra. However, these high E_u lines (349907.88 MHz, 351232.91 MHz) are fully blended but it helps us estimate the range of column density upper limits.

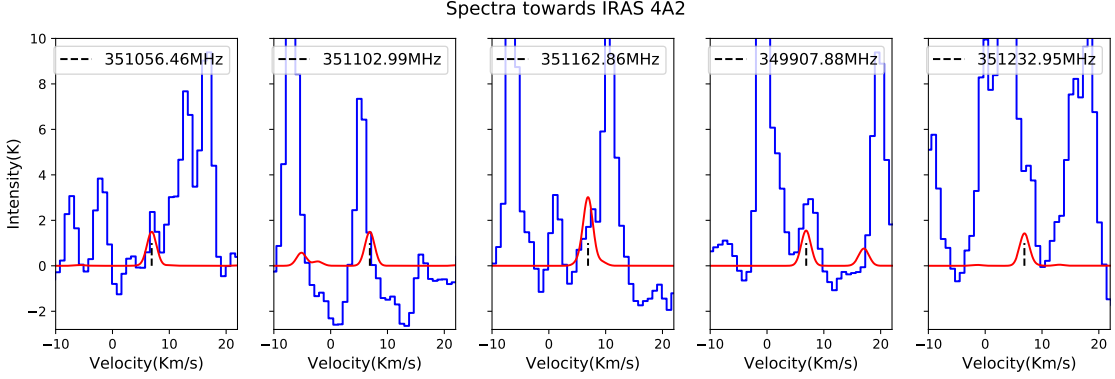


Figure B.1. LTE synthetic spectra (red) for an excitation temperature of 300 K overplotted on observed spectra (blue) towards IRAS 4A2.

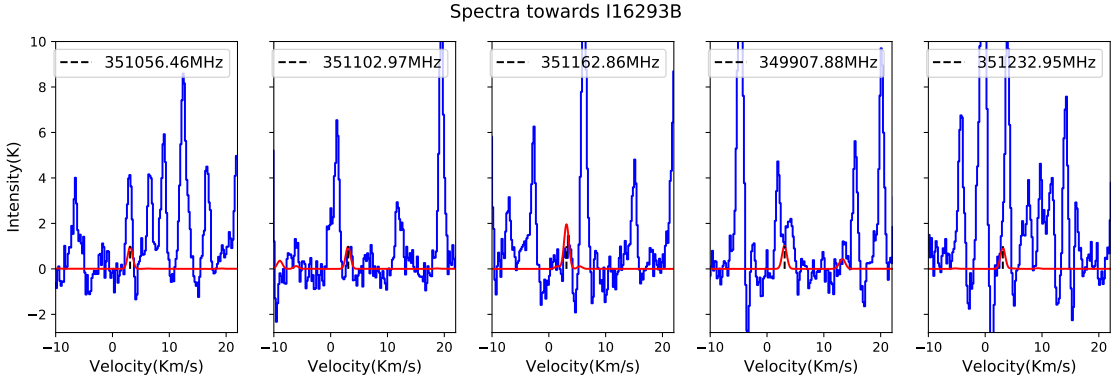


Figure B.2. Similar to Figure B.1, spectra towards IRAS I16293B.

C. FULL LIST OF MC TRANSITIONS

The Table 4 in the text shows the list of representative transitions. Multiple transitions are present around those frequencies. Table C.1 list multiple transitions around the frequencies.

REFERENCES

- Aikawa Y., Wakelam V., Garrod R. T., Herbst E., 2008, *ApJ*, 674, 984
- Altwegg, K., Balsiger, H., Bar-Nun, A., et al. 2016, *Sci. Adv.*, 2, e1600285
- Bottinelli, S., Ceccarelli, C., Lefloch, B., et al. 2004, *ApJ*, 615, 354
- Cernicharo, J., N. Marcelino, N., Roueff, E. et al., 2012, *ApJL*, 759:L43
- Das A., Majumdar L., Sahu D., Gorai P., Sivaraman B., Chakrabarti S. K., 2015, *ApJ*, 808, 21
- Das A., Majumdar L., Chakrabarti S. K., Sahu D., 2015a, *New Astron.*, 35, 53
- Das, A., Sahu, D., Majumdar, L., & Chakrabarti, S. K. 2016, *MNRAS*, 455, 540
- Demyk, K., Wlodarczak, G., & Dartois, E. 2004, in *Semaine de Áastrohysique Francaise*, ed. F. Combes, D. Barret, T. Contini, F. Meynadier, & L. Pagani (SF2A-2004; Les Ulis: EDP-Sciences.), 493
- Drozdovskaya M. N., van Dishoeck E. F. et al. 2019, *MNRAS*, 490, 5079
- Garrod, R. T., & Herbst, E. 2006, *A&A*, 457, 927
- Garrod, R. T. 2013, *ApJ*, 765, 60.
- Gorai, P., et al. 2020, arXiv:2003.09188

Table C.1. Methyl carbamate transitions

Species	Transition (N Ka Kc v F*)	Frequency (MHz) (Error)	Eu (K)	$A_{ij}(s^{-1})$
H ₂ NCO ₂ CH ₃	(20,15,5,3,20 - 19,14,6,3,19)	349907.88 (0.0157)	322.69	9.22E-4
H ₂ NCO ₂ CH ₃	(20,15,6,3,20 - 19,14,5,3,19)	349907.88 (0.0157)	322.69	9.22E-4
H ₂ NCO ₂ CH ₃	(20,15,5,3,21 - 19,14,6,3,20)	349907.92 (0.0157)	322.69	9.25E-4
H ₂ NCO ₂ CH ₃	(20,15,6,3,21 - 19,14,5,3,20)	349907.92 (0.0157)	322.69	9.25E-4
H ₂ NCO ₂ CH ₃	(20,15,5,3,19 - 19,14,6,3,18)	349907.92 (0.0157)	322.69	9.22E-4
H ₂ NCO ₂ CH ₃	(20,15,6,3,19 - 19,14,5,3,18)	349907.92 (0.0157)	322.69	9.22E-4
H ₂ NCO ₂ CH ₃	(18,16,2,2,18 - 17,15,2,2,17)	351056.43 (0.0098)	147.42	3.29E-3
H ₂ NCO ₂ CH ₃	(18,16,2,2,17 - 17,15,2,2,16)	351056.46 (0.0098)	147.42	3.11E-3
H ₂ NCO ₂ CH ₃	(18,16,2,2,19 - 17,15,2,2,18)	351056.46 (0.0098)	147.42	1.11E-3
H ₂ NCO ₂ CH ₃	(18,16,3,1,18 - 17,15,3,1,17)	351102.99 (0.0090)	147.38	1.11E-3
H ₂ NCO ₂ CH ₃	(18,16,3,1,17 - 17,15,3,1,16)	351103.01 (0.0090)	147.38	3.12E-3
H ₂ NCO ₂ CH ₃	(18,16,3,1,19 - 17,15,3,1,18)	351103.02 (0.0090)	147.38	3.48E-3
H ₂ NCO ₂ CH ₃	(18,16,2,0,18 - 17,15,3,0,17)	351162.83 (0.0092)	147.42	1.11E-3
H ₂ NCO ₂ CH ₃	(18,16,3,0,18 - 17,15,2,0,17)	351162.83 (0.0092)	147.42	3.29E-3
H ₂ NCO ₂ CH ₃	(18,16,2,0,17 - 17,15,3,0,16)	351162.86 (0.0092)	147.42	3.12E-3
H ₂ NCO ₂ CH ₃	(18,16,3,0,17 - 17,15,2,0,16)	351162.86 (0.0092)	147.42	3.12E-3
H ₂ NCO ₂ CH ₃	(18,16,2,0,19 - 17,15,3,0,18)	351162.86 (0.0092)	147.42	3.48E-3
H ₂ NCO ₂ CH ₃	(18,16,3,0,19 - 17,15,2,0,18)	351162.86 (0.0092)	147.42	3.48E-3
H ₂ NCO ₂ CH ₃	(22,14,9,3,22 - 21,13,8,3,21)	351232.91 (0.0124)	329.02	7.93E-4
H ₂ NCO ₂ CH ₃	(22,14,8,3,22 - 21,13,9,3,21)	351232.91 (0.0124)	329.02	7.93E-4
H ₂ NCO ₂ CH ₃	(22,14,9,3,23 - 21,13,8,3,22)	351232.95 (0.0124)	329.02	7.95E-4
H ₂ NCO ₂ CH ₃	(22,14,8,3,23 - 21,13,9,3,22)	351232.95 (0.0124)	329.02	7.95E-4
H ₂ NCO ₂ CH ₃	(22,14,8,3,21 - 21,13,9,3,20)	351232.95 (0.0124)	329.02	7.93E-4
H ₂ NCO ₂ CH ₃	(22,14,9,3,21 - 21,13,8,3,20)	351232.95 (0.0124)	329.02	7.93E-4

*The quantum numbers (QN) are mentioned as N Ka Kc v F . The ‘F’ QN can also denote an A or E state as in the case for MC.

- Guillemin, J.-C., 2014, BIO Web of Conferences, 2,04002
- Haupa, K. A., Tarczay, G., & Lee, Y.-P. 2019, J. Am. Chem. Soc., 141, 11614.
- Hickson, K. M., Loison, J.-C., & Wakelam, V. 2016, Chem. Phys. Lett., 659, 70
- Ilyushin, V., Alekseev, E., Demaison, J., Kleiner, I., J. Mol. Spectrosc. 240 (2006)
- Jiménez-Serra, I. et al., 2020, section 3.3, Memo 20-01, SKA1 Beyond 15GHz: The Science case for Band 6.
- Jørgensen J. K. et al., 2016, A&A, 595, A117
- Jørgensen J. K. et al., 2018, A&A, 620, A170
- Jørgensen, J. K., Bourke, T. L., Nguyen Luong, Q., & Takakuwa, S. 2011, A&A, 534, A100
- Khare, B.N., Sagan, C., Ogino, H., Nagy, B., Er, C., et al. 1986, 68, 176- 84
- Kuan, Y. J., Charnley, S. B., Huang, H. C., Tseng, W. L., & Kisiel, Z. 2003, ApJ, 593, 848
- Lattelais, M., Pauzat, F., Ellinger, Y., & Ceccarelli, C. 2009, ApJ, 696, L133
- Lattelais, M., Risset, O., Pilm, J., et al. 2011, Int. J. Quantum Chem., 111, 1163
- Lee, C-W., Kim, J-K., Moon, E-S. et al., 2009, 697:428435.
- Ligterink, N. F. W., Terwisscha van Scheltinga, J. et al. 2018, MNRAS 480, 3628
- Loison, J.-C., Agúndez, M., Marcelino, N., et al. 2016, MNRAS, 456, 4101
- Loison, J.-C., Agúndez, M., Wakelam, V., et al. 2017, MNRAS, 470, 4075
- Loomis, Ryan A., McGuire, Brett A., Shingledecker, C. et al. 2015, ApJ, 799:34.
- Looney, L. W., Mundy, L. G., & Welch, W. J. 2000, ApJ, 529, 477
- López-Sepulcre, A., Sakai, N., Neri, R., Imai, M. et al. 2017, A&A, 606, A121
- McGuire, Brett A. et al., 2018, Astronomical Society of the Pacific, Science with a Next-Generation Very Large Array ASP Conference Series, Monograph 7 Eric J. Murphy, ed.
- Miller, S.L., 1953, Science, 117(3046), 528-529
- Müller H. S. P., Thorwirth S., Roth D. A., Winniewisser G., 2001, A&A,370, L49.
- Müller H. S. P., Schlöder F., Stutzki J., Winniewisser G., 2005, J. Mol. Struct., 742, 215

- Ortiz-León, G N., Loinard L., Dzib S A. et. al. 2018, ApJ, 865:73
- Persson, M. V., Jrgensen, J. K., & van Dishoeck, E. F. 2012, A&A, 541, A39
- Pickett H. M., Poynter R. L., Cohen E. A., Delitsky M. L., Pearson J. C., Müller H. S. P., 1998, J. Quant. Spectrosc. Radiat. Transfer, 60, 883.
- Quénard, D., Jiménez-Serra, I., Viti, S., Holdship, J., & Coutens, A. 2018, MNRAS, 474, 2796
- Reipurth, B., Rodrguez, L. F., Anglada, G., & Bally, J. 2002, AJ, 124, 1045
- Ruaud M., Wakelam V., Hersant F., 2016, MNRAS, 459, 3756
- Sahu D., Das A., Majumdar L., Chakrabarti S. K., 2015, New Astron., 38, 23
- Sahu, D., Liu, S.-Y., Su, Y.-N., et al. 2019, ApJ, 872, 196
- Sánchez-Monge, Á, Schilke, P., Ginsburg, A. et al. 2018, A&A, 609, A101
- Snyder, L. E., Lovas, F. J., Hollis, J. M., et al. 2005, ApJ, 619, 914
- Su, Y-N., Liu, S-Y., Li, Z-Y. et al. 2019, ApJ, 885:98
- Suzuki, T., Liton Majumdar, L., Ohishi, M. et al. 2018, ApJ, 863:51
- Taquet, V., Lopez-Sepulcre, A., Ceccarelli, C., et al. 2015, ApJ, 804, 81
- Toshiki, K., Hiroshi, N., 2017, Scientific Reports, 7, 636
- Vidal T. H. G., Loison J.-C., Jaziri A. Y., Ruaud M., Gratier P., Wakelam V., 2017, MNRAS, 469, 435
- Viti, S., Collings, M. P., Dever, J. W., McCoustra, M. R. S., & Williams, D. A. 2004, MNRAS, 354, 1141
- Wakelam V., Vastel C., Aikawa Y., Coutens A., Bottinelli S., Caux E., 2014, MNRAS, 445, 2854
- Wakelam, V., Loison, J.-C., Herbst, E., et al. 2015, ApJS, 217, 20
- Wakelam, V., Loison, J. C., Mereau, R., & Ruaud, M. 2017, MolAs, 6, 22.
- Wakelam, V., Chapillon, E., Dutrey, A. et al., 2019, MNRAS 484, 15631573.
- Zucker, C., Schlafly, E.F., Speagle, S.F., Green, G.M., et. al., 2018, ApJ, 869:83